

# Guided transmission of $\text{Ne}^{7+}$ ions through nanocapillaries in insulating polymers: Scaling laws for projectile energies up to 50 keV

N. Stolterfoht and R. Hellhammer

*Helmholtz-Zentrum Berlin für Materialien und Energie, Glienickerstr. 100, D-14109 Berlin, Germany*

Z. Juhász and B. Sulik

*Institute of Nuclear Research (ATOMKI), H-4001 Debrecen, Hungary*

V. Bayer and C. Trautmann

*Helmholtz-Zentrum für Schwerionenforschung (GSI), Materialforschung, D-64291 Darmstadt, Germany*

E. Bodewits, A. J. de Nijs, H. M. Dang, and R. Hoekstra

*KVI Atomic Physics, University of Groningen, 9747 AA Groningen, The Netherlands*

(Received 3 March 2009; published 17 April 2009)

The guiding of multiply charged  $\text{Ne}^{7+}$  ions through nanocapillaries in highly insulating polymers was investigated. Highly parallel capillaries with a density of  $\approx 10^7 \text{ cm}^{-2}$  and diameters of  $\approx 100 \text{ nm}$  were utilized. The widths of the angular profiles were measured for  $\text{Ne}^{7+}$  ions transmitted through the capillaries. Moreover, the fractions of transmitted ions were measured as a function of the capillary tilt angle. The results were used to evaluate the characteristic guiding angle, which is a measure of the *guiding power* specifying the ability of a material to guide ions. Results for the polyethylene terephthalate (PET) and polycarbonate (PC) samples were compared to verify the role of the material of the capillary wall. Relatively high projectile energies of up to 50 keV were used to extend the validity of previous scaling laws based on the projectile charge-to-energy ratio. The profile widths and the guiding angles for both polymers are found to compare well with the scaling laws showing that PET and PC have nearly equal guiding properties.

DOI: [10.1103/PhysRevA.79.042902](https://doi.org/10.1103/PhysRevA.79.042902)

PACS number(s): 61.85.+p, 34.50.Fa, 32.80.Fb

## I. INTRODUCTION

In past few years, the guiding of highly charged ions through capillaries of mesoscopic dimensions has received a great deal of attention. Pioneering results for ion transmission through capillaries have been achieved with conducting materials [1–3]. First studies of the guiding phenomena have been performed with capillaries in highly insulating polyethylene terephthalate (PET) polymers [4–9]. For capillaries tilted with respect to the incident-beam direction, the ion guiding involves the deposition of positive charges at the inner wall of the capillaries in a self-organizing process [4]. The charge deposition in the entrance region continues until the electric field becomes sufficiently large to deflect the ions in the directions of the capillary exit. For the subsequent ions the charge deposition is reduced to an amount just necessary to maintain the ion guiding.

Since the ions are deflected at relatively large distances from the capillary wall, the transmission of highly charged ions occurs with negligible charge exchange. Thus, the major fraction of ions are guided through the capillary in its incident charge state. Due to the increasing interest in this subject, several laboratories started investigations of capillary guiding using PET [10–12], polycarbonate (PC) [13],  $\text{SiO}_2$  [14], and  $\text{Al}_2\text{O}_3$  [15–19]. Moreover, electrons were used as projectiles guided through capillaries in  $\text{Al}_2\text{O}_3$  [20] and PET [21]. Also, single-glass capillaries [22–24] have been applied with the intention to produce submicrometer-sized beams that can be used for surface modification or to selectively damage the different constituents of biological cells.

Monte Carlo simulations [25,26] have explicitly shown that most of the deposited charge is located near the entrance region. Evidence has been provided that the discharge of the entrance patch is governed by a strongly nonlinear law [27,28]. In recent studies [29–31] particular attention has been devoted to dynamic properties of the capillary guiding involving additional weaker patches temporarily produced behind the entrance patch (Fig. 1). However, at equilibrium, the electric field within the inner part of the capillary plays a minor role, since an infinite homogeneously charged tube is field free (similarly as in a Faraday cage). Nevertheless, due to the loss of symmetry at the end of the capillary an electric field is produced by the charges deposited within the capil-

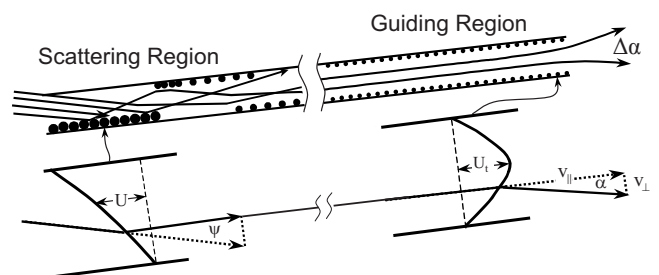


FIG. 1. Capillary guiding of ions in an insulating capillary. In the entrance region the main charge patch is created that deflects the ions to the capillary exit. The quantity  $U$  is a characteristic potential across the capillary diameter and  $\psi$  is the tilt angle. The exit region is affected by a symmetric potential of depth  $U_t$  in which the ions can gain perpendicular velocity  $v_{\perp}$ . More information is given in Ref. [28].

lary. Thus, in the exit region, the ions are defocused, leading to a widening of the transmission profile.

The capability of insulating capillaries to guide ions is referred to as the *guiding power* [32,33]. The fraction  $f(\psi)$  of transmitted ions at equilibrium generally decreases with tilt angle  $\psi$ . The guiding power can be quantized by the *guiding angle*  $\psi_c$  for which the normalized transmission fraction drops as  $f(\psi_c)/f(0)=1/e$ . This definition of the guiding angle has been motivated by the observation that the tilt-angle dependence of the transmitted fraction can well be described by a Gaussian function [6,8]. The guiding angle and the angle due to the width of the transmission profile (also referred to as characteristic angles) may be governed by the dominant charge patch in the entrance region. Thus, a linear relationship between the characteristic angles is expected.

Systematic studies of the capillary guiding in PET have been performed with a variety of highly charged ions to determine the profile width and guiding angle. Both characteristic angles were found to follow a unique scaling law when plotted as a function of the projectile charge-to-energy ratio [28,34]. In particular, a linear relationship was found between the characteristic angles suggesting that they are produced by the same charge patch in the entrance region.

The guiding angle is primarily governed by the ability of the material to store charges in the entrance patch, whereas the width of the transmission profile depends on further capillary parameters. Recently, it has been shown [34] that the width of the transmission profile depends on the capillary density, since it may be enhanced by the charges in neighboring capillaries [26]. Also, it is expected that the capillary material has a decisive influence on the ability to store charge in the entrance region. Indeed, varying results for the guiding angle and profile width were reported by different laboratories [10,12–15,17,19].

In the present work, we study the polymers PET and PC to verify the influence of the capillary material on the capillary guiding. The guiding angle and profile width of the transmitted ions were measured as a function of the tilt angle. The primary goal was the verification of the scaling laws for higher  $\text{Ne}^{7+}$  energies of up to 50 keV, corresponding to the projectile charge-to-energy ratio down to  $0.14 \text{ kV}^{-1}$ . The characteristic angles of both polymers PET and PC were found to agree with the previous scaling law, establishing its validity for a larger energy range.

## II. BASIC FORMALISM

Figure 1 shows schematics of the capillary guiding in conjunction with the parameters used in the present analysis. We consider the doubly differential ion yield  $dY(\theta, \phi)/d\Omega$ , where  $\theta$  and  $\phi$  are angles defined relative to the incident beam as angular deviations in the horizontal and vertical directions, respectively. Previous model calculations [6,8] have shown that the angular distribution of the transmitted ions at  $\phi=0$  may be described by a Gaussian-type function

$$\frac{dY(\theta)}{d\Omega} = \frac{dY_{\max}}{d\Omega} \exp\left(-\frac{\sin^2 \alpha}{\sin^2 \alpha_t}\right), \quad (1)$$

where  $dY_{\max}/d\Omega$  is the maximum yield for  $\alpha=0$ . The angle  $\alpha_t$  represents the width of the emission profile. The ion emis-

sion angle  $\alpha = \psi - \theta$  is measured relative to the capillary axis. As the observation angle  $\theta$ , the tilt angle  $\psi$  is defined relative to the beam direction (Fig. 1).

Next, we consider the total yield  $Y(\psi)$  of the transmitted ions obtained by integration over the angles  $\theta$  and  $\phi$ . The total yield  $Y(\psi)$  can be converted to the fraction  $f(\psi)$  of transmitted ions, which is defined as the ratio of transmitted to incident ions. Similarly as the transmission profile, the fraction of transmitted ions can be expressed by a Gaussian-type function [5,6]:

$$f(\psi) = \frac{Y(\psi)}{Y_{in}} = f_0 \exp\left(-\frac{\sin^2 \psi}{\sin^2 \psi_c}\right), \quad (2)$$

where  $f_0 \leq 1$  is the transmitted fraction at  $\psi=0$ . The quantity  $\psi_c$  can be identified as the guiding angle, which is a measure of the guiding power of the capillary. It is obtained from the drop of the transmitted ion fraction to the  $1/e$  value, as mentioned before.

It has recently been shown [28,34] that the profile width angle  $\alpha_t$  and the guiding angle  $\psi_c$  can be obtained from the simple expressions

$$\psi_c \approx \sin \psi_c = \sqrt{U \frac{q}{E_p}} \quad \text{and} \quad \alpha_t \approx \sin \alpha_t = \sqrt{U_t \frac{q}{E_p}}, \quad (3)$$

where  $q$  and  $E_p$  are projectile charge and energy, respectively. Note that the relevant angles are sufficiently small so that one may set  $\sin \psi_c \approx \psi_c$  and  $\sin \alpha_t \approx \alpha_t$ . The free-model parameter  $U$  is an effective potential difference across the capillary diameter produced by the charge deposited in the entrance region. Similarly, the free-model potential  $U_t$  is responsible for the ion defocusing in the exit region of the capillary (Fig. 1). If  $U_t$  is produced by charges deposited in the entrance region, the exit potential is expected to be symmetric [26]. On the other hand, if it is produced by charges transported to the exit region, it may have a shape similar to that of the entrance potential [31]. In the latter case, however, Eq. (3) remains valid.

The first expression in Eq. (3) implies that for  $\psi = \psi_c$  the perpendicular energy  $E_{\perp} = E_p \sin^2 \psi$  of the incident ion is equal to the potential energy  $qU$ . For  $\psi > \psi_c$  the quantity  $E_{\perp}$  is larger than  $qU$  and the incident ion is lost by deposition onto the capillary wall. For  $\psi < \psi_c$  the ions are deflected and can be transmitted through the capillary. Similar conditions are valid for the second part in Eq. (3).

From the expressions in Eq. (3) we keep in mind that the profile width and the fraction of transmitted ions are governed by expressions which differ only by the potentials  $U$  and  $U_t$ . Hence, the results for the profile width and the guiding angle are expected to follow the same scaling law. We shall come back to this point in the section devoted to the analysis of the experimental results (Sec. IV).

## III. EXPERIMENTAL METHOD

The experiments were conducted in an ultrahigh vacuum chamber mounted at the 14 GHz electron cyclotron resonance (ECR) ion source of the ZERNIKE-LEIF facility at the KVI Groningen (Netherlands) [31,35]. For the present

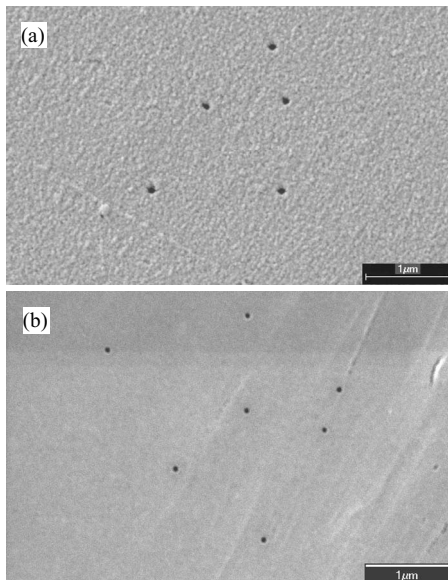


FIG. 2. Scanning electron microscopy images showing openings of capillaries. Note the scale of  $1 \mu\text{m}$  on the right-hand bottom. The sample in (a) prepared with PET at HMI contains capillaries with a diameter of  $\sim 100 \text{ nm}$  and a density of  $4 \times 10^6 \text{ cm}^{-2}$ . The sample in (b) prepared at GSI with PC contains capillaries with a diameter of  $\sim 60 \text{ nm}$  and a density of  $10^7 \text{ cm}^{-2}$ . In (a) and (b) the foil surface is covered with a gold layer of 30 and 10 nm thicknesses produced by an evaporation and a sputtering technique, respectively.

capillary experiments we could not bake the chamber so that the base pressure in the chamber was a few  $10^{-8}$  mbar. The chamber was operated on high voltage to allow for the deceleration of the incident  $\text{Ne}^{7+}$  ions from  $\sim 50 \text{ keV}$  to an energy as low as  $3 \text{ keV}$  along a set of lenses. The current was as high as a few nA. The beam was collimated to a diameter of  $1 \text{ mm}$  with a divergence better than  $0.2^\circ$  full width at half maximum (FWHM).

For the experiments, cylindrical capillaries in insulating polymers were prepared in the Ionenstrahllabor (ISL) at the former Hahn-Meitner-Institut (HMI) (now Helmholtz-Zentrum Berlin) and the Department of Materialforschung of the Helmholtz-Zentrum für Schwerionenforschung (GSI). At HMI the capillaries were produced in PET by etching tracks of  $250 \text{ MeV}$  krypton ions [32]. The PET foil of  $12 \mu\text{m}$  thickness contains capillaries with a density of  $4 \times 10^6 \text{ cm}^{-2}$  and a diameter of  $100 \pm 10 \text{ nm}$ . A scanning electron microscopy image of the PET surface is given in Fig. 2(a). At GSI capillaries were produced in PC samples by etching the tracks of  $2 \text{ GeV}$  gold ions [36]. The PC foil of  $10 \mu\text{m}$  thickness contains capillaries with a density of  $10^7 \text{ cm}^{-2}$  and a diameter of  $60 \pm 6 \text{ nm}$  as shown in Fig. 2(b).

The density of the capillaries in both polymers implies a geometric opening of  $\sim 0.03\%$ . The mean distance was about  $3 \mu\text{m}$  between neighboring capillaries so that an overlap of adjacent capillaries is unlikely to happen. (Note that for the images in Fig. 2 we selected sample pieces which exhibit a relatively large number of capillaries.) To avoid the macroscopic chargeup of the sample surfaces, gold was deposited

on their front and the back sides, forming films of 10 and 30 nm thicknesses on PC and PET, respectively.

With the conducting surfaces it was possible to verify the insulator properties of the capillaries by applying a high voltage between the front and back sides of a PET foil. A voltage break through was found to start at about  $1.1 \text{ kV}$ . Since, the PET foil has a thickness of  $12 \mu\text{m}$ , the breakthrough sets in at the electric field of  $\sim 0.1 \text{ V/nm}$ . Thus, for a capillary of  $100 \text{ nm}$  diameter, the maximum voltage across the inner opening of the capillary is  $\sim 10 \text{ V}$ . Note that this value does not apply for the bulk of the PET sample, but for the inner surface of the capillaries. Hence,  $10 \text{ V}$  is an upper limit for the potentials created in the entrance and exit regions of the capillaries.

Care was taken to minimize the nonparallelism of the capillaries. For the production of the ion tracks, well-collimated ion beams of low divergence were used. The high energy of the ions ensured that the angular spread due to Rutherford scattering in the polymer is negligible. Within the following experiments the angular spread of the capillary inclination was estimated to be  $\lesssim 0.2^\circ$  FWHM, which was smaller than the aspect angles of  $\sim 0.45^\circ$ . This small FWHM is a decisive condition for the present experiments where relatively high projectile energies were used. With the PET capillaries experiments were performed using  $\text{Ne}^{7+}$  ions of  $3 \text{ keV}$ , whereas with the PC capillaries higher energies of  $10$ ,  $20$ , and  $50 \text{ keV}$  were applied. For  $50 \text{ keV}$   $\text{Ne}^{7+}$  the characteristic guiding angle is of the same order of magnitude as the aspect angle and the capillary inclination. It is evident that such a small guiding angle can only be measured adequately with highly parallel capillaries.

The PET target foils were mounted on circular frames with an inner diameter of  $7 \text{ mm}$  which, in turn, were mounted on a target ladder. It can hold four samples, from which two were used in the experiment. The target ladder was fixed at a goniometer, which allowed for tilting the capillaries relative to the incident beam in two directions specified by the angles  $\psi$  and  $\varphi$ . The tilt angle  $\psi$  was varied to change the angle between the incident beam and the capillary axis. The azimuthal angle  $\varphi$  was kept constant after its zero value was determined. The target could be moved by the goniometer in two dimensions with respect to the incident ion beam. Thus, within the target area the ion beam could be positioned to spots not used before in the experiments.

The ions transmitted through the capillaries were measured using an electrostatic  $180^\circ$  analyzer, which was rotated by the angle  $\theta$  in the same plane as the tilt angle  $\psi$ . The entrance diaphragm of the analyzer has an opening of  $0.4 \text{ mm}$  and was located  $75 \text{ mm}$  away from the target position. Hence, the angular resolution of the analyzer is obtained as  $0.2^\circ$  FWHM. With the analyzer a Gaussian-type angular profile with a FWHM of  $0.4^\circ$  was measured for the direct incident beam (without the capillary target). This width is a composition of the beam width, its divergence, and the angular resolution of the analyzer. The energy resolution of the analyzer was  $0.5\%$ , which was high enough to separate the charge states of the transmitted ions. In the following we study exclusively  $\text{Ne}^{7+}$  ions transmitted through the capillary in their incident charge state.

**IV. EXPERIMENTAL RESULTS**

In this section, we discuss transmission profiles which represent the transmitted ion intensity as a function of the observation angle  $\theta$  (defined relative to the incident-beam direction). First, we present profiles for 3 keV  $\text{Ne}^{7+}$  ions, which have frequently been used in previous studies [4–6,27,34]. During the experiment an important parameter was the charge  $Q_d$  deposited at the front surface of the capillary sample (covered with Au). This charge is simply obtained by time integration of the incident ion current. In this work, all results were achieved under equilibrium conditions, i.e., for sufficient charge accumulation at which the transmitted ion intensity does not change any more. The dynamic properties of the ion guiding in the pre-equilibrium stage are described elsewhere [31].

Figure 3 depicts transmission profiles which were normalized to the deposited charge of  $Q_d=1$  nC. Data were obtained for an untilted foil with  $\psi=0^\circ$  and for a tilt angle of  $\psi=5^\circ$ . We note that the intensity of the transmission profiles decreases with increasing tilt angle. This decrease is governed by the guiding angle  $\psi_c$  at which the intensity of the transmission profile drops to the value of  $1/e$ . For Fig. 3 the guiding angle is determined to be  $5.2^\circ$ . In Fig. 4 transmission profiles obtained with the PC sample are presented. The data are taken for  $\text{Ne}^{7+}$  with relatively high impact energies of 10, 20, and 50 keV. The data were measured within the tilt-angle range of  $0^\circ - 2.5^\circ$ . The resulting guiding angles will be discussed further below.

To analyze the experimental results we make use of Eq. (1) in accordance with previous observations [4–7] showing that a transmission profile can well be fitted by the Gaussian-type function. When fitting the experimental data the width  $\alpha_t$  of the Gaussian function is treated as an adjustable parameter. As seen from Figs. 3 and 4 the measured transmission profiles agree well with the Gaussian fit function given by Eq. (1).

At this point we introduce a change in the definition of the profile width. In the literature it is common practice to use

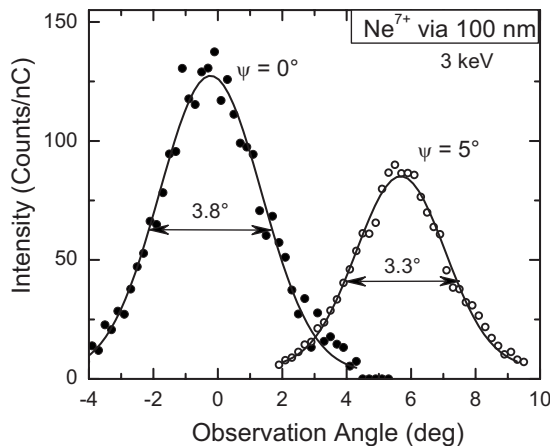


FIG. 3. Transmission profiles of  $\text{Ne}^{7+}$  ions through capillaries with a diameter of 100 nm in PET measured for tilt angles  $\psi=0^\circ$  and  $5^\circ$ . The incident energy was 3 keV. The experimental data were fitted by Gaussian functions given as solid lines.

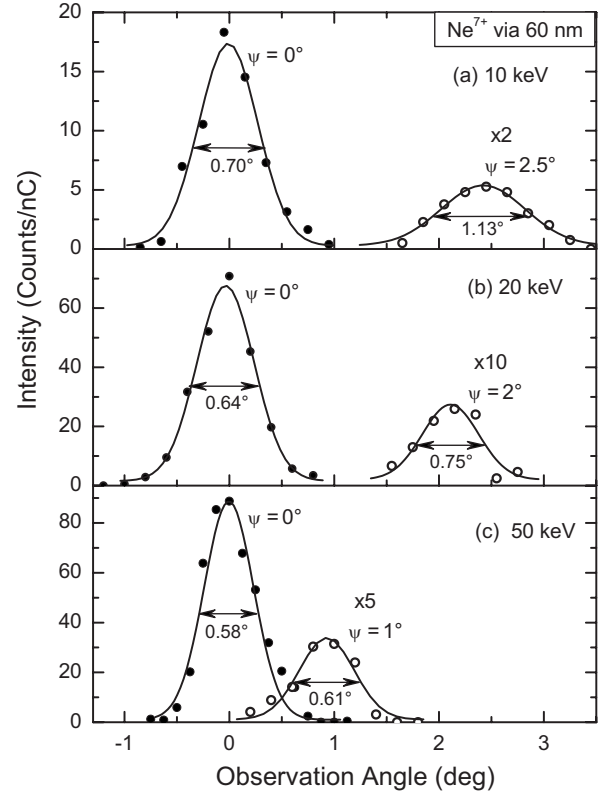


FIG. 4. Transmission profiles of  $\text{Ne}^{7+}$  ions plotted as functions of the observation angle  $\theta$ . The ions were transmitted through capillaries with a diameter of 60 nm in a PC sample. The tilt angle  $\psi$  was varied in the range of  $0^\circ - 2.5^\circ$ . The incident energies were 10, 20, and 50 keV. The experimental data are fitted by Gaussian functions given as solid lines. Note that some peaks are enhanced by the factors indicated at the graphs.

the FWHM  $\sigma_t$ , which is obtained by  $\sin \sigma_t = 2\sqrt{\ln 2} \sin \alpha_t$ . In Figs. 3 and 4 the fit results of the FWHM  $\sigma_t$  are given at the transmission profiles. The width is seen to increase with the tilt angle  $\psi$ . Also, Fig. 4 indicates that the profile width for nonzero tilt angles decreases with increasing projectile energy; e.g., for 10 keV the width amounts to  $\sigma_t \approx 1.13^\circ$ , which drops to  $0.61^\circ$  at 50 keV. The energy dependence of the profile width can be reproduced by model calculations as will be shown in the section devoted to the scaling laws (Sec. V).

Next, we determine the fraction of transmitted ions by integration of the transmission profiles. In the present experiments using an electrostatic spectrometer, the transmission profiles were measured for  $\phi=0$  as a function of the observation angle  $\theta$ . Since only the single  $\phi=0$  angle was measured, an extrapolation in the unobserved  $\phi$  region was required. This was done assuming that the profile in  $\phi$  direction can be fitted by a Gaussian function as well as for the  $\theta$  direction (Figs. 3 and 4). Hence, the integration can be performed analytically:

$$Y(\psi) = \frac{\pi}{4 \ln 2} \frac{dY_{\max}}{d\Omega} \sigma_\theta \sigma_\phi, \quad (4)$$

where  $\sigma_\theta$  and  $\sigma_\phi$  are the FWHMs in  $\theta$  and  $\phi$  directions, respectively. Since in the experiments no information was

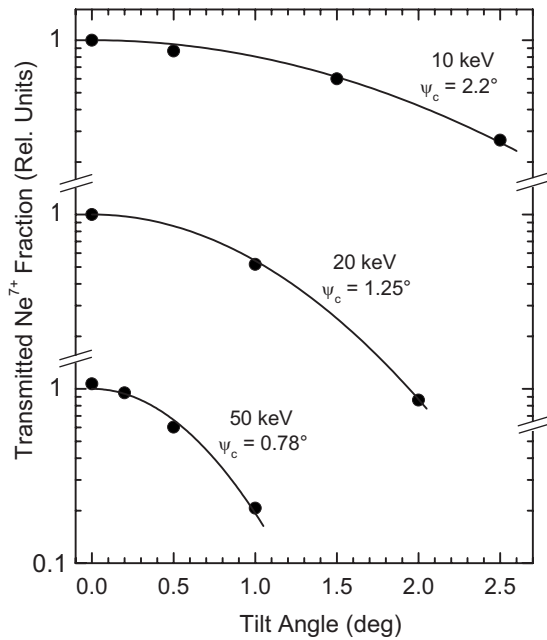


FIG. 5. Fraction  $f(\psi)$  of transmitted  $\text{Ne}^{7+}$  ions derived from the transmission profiles given in Fig. 4, where  $\psi$  is the tilt angle. The data given for the projectile energies of 10, 20, and 50 keV were normalized to unity for  $\psi=0$ . The solid lines represent Gaussian fit functions. The guiding angle  $\psi_c$ , given at each graph, characterizes the  $1/e$  drop in the corresponding Gaussian function.

available about  $\sigma_\phi$ , we have set  $\sigma_\phi = \sigma_\theta = \sigma_t$  for simplicity. More details about the integration procedure are given in Ref. [28].

The total yield  $Y(\psi)$  was converted to the fraction  $f(\psi)$  of transmitted ions by means of Eq. (2). In Fig. 5 the transmitted fractions of  $\text{Ne}^{7+}$  ions are plotted as a function of the tilt angle  $\psi$ , which shows that this fraction decreases with the tilt angle. For the further analysis, we make use of Eq. (2) predicting that the experimental fraction of transmitted ions can be fitted by the Gaussian-type function [6,8,20]. The fit procedure determines the characteristic tilt angle  $\psi_c$  referred to as *guiding angle*.

Figure 5 indicates that the Gaussian fits compare well with the experimental data of the transmitted ion fractions. The guiding angles obtained from the fits are given at the corresponding curves. In Sec. V, the guiding angles will be analyzed.

## V. SCALING LAWS

In this section, we compare all data achieved for the guiding angle  $\psi_c$  and the profile width  $\sigma_t$  with the results of scaling laws found previously. Following the prediction of Eq. (3), the characteristic angles are plotted as a function of  $(q/E_p)^{1/2}$ , where  $q/E_p$  is the charge-to-energy ratio of the projectile. In Fig. 6 the results are presented showing that the data sets follow universal curves. It should be pointed out that the presentation of the previous data sets is limited to the projectiles  $\text{Ne}^{7+}$  and  $\text{Ne}^{9+}$ . As explicitly shown before [28,34], the characteristic angles for quite different projec-

tiles, such as  $\text{Xe}^{25+}$  and  $\text{Ar}^{13+}$ , follow the same scaling law as depicted in Fig. 6. This indicates that the  $(q/E_p)^{1/2}$  is an appropriate scaling parameter for the characteristic angles.

However, only one previous data point existed at the higher limit of the  $(q/E_p)^{1/2}$  range of 0.37–8.4  $\text{kV}^{-1/2}$ , in which the present results with the PC capillaries were acquired. This range corresponds to the high energies of 10, 20, and 50 keV for  $\text{Ne}^{7+}$  (Fig. 4). Moreover, the data point at 1.53  $\text{kV}^{-1/2}$  corresponds to the measurement with the PET capillaries using 3 keV  $\text{Ne}^{7+}$  ions (Fig. 3). The present results are in excellent agreement with the previous data point. The PC results for  $(q/E_p)^{1/2} = 0.84 \text{ kV}^{-1/2}$  (10 keV  $\text{Ne}^{7+}$ ) compare well with the corresponding value obtained previously with PET. This shows that the guiding properties of PC and PET are practically the same.

We should mention that the previous data [28] (and the scaling rules) have been obtained with a capillary diameter of 200 nm, whereas the present results were measured with diameters of 60 and 100 nm. We also performed measurements with larger capillary diameter (in PET) partially given in Ref. [31]. Our experiments suggest that at least the guiding power was greatly independent of the capillary diameter. However, the profile width may depend on specific parameters such as the capillary diameter and density [34]. We shall postpone these open questions to a future study.

With constant potentials  $U$  and  $U_p$ , the expressions in Eq. (3) predict a linear relation between the characteristic angles and  $(q/E_p)^{1/2}$ . Indeed, in Fig. 6 the experimental data exhibit

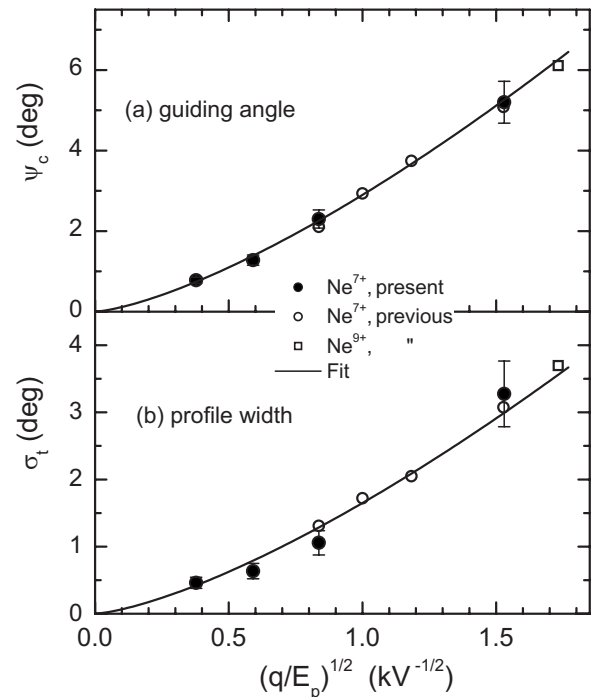


FIG. 6. Scaling laws for the guiding angle  $\psi_c$  and the width  $\sigma_t$  (FWHM) of the transmission profile, shown in (a) and (b), respectively. The angles are plotted as a function of the square root of the charge-to-energy ratio  $q/E_p$ . The present results are given as solid circles. The previous data, shown as open circles and squares, are taken from Ref. [28]. The solid lines represent fit functions discussed in the text.

a nearly linear increase with the scaling parameter. However, there are deviations from the linear dependence, in particular, in the small  $(q/E_p)^{1/2}$  range, in which the present data were taken. Improved agreement between the experimental data and universal curves is achieved with

$$\psi_c = u \left( \frac{q}{E_p} \right)^{0.7} \quad \text{and} \quad \sigma_t = u_t \left( \frac{q}{E_p} \right)^{0.7}, \quad (5)$$

where  $u$  and  $u_t$  are treated as adjustable parameters. In Fig. 6 the fit results are shown as solid lines deduced with the values  $u=2.9 \text{ deg kV}^{0.7}$  and  $u_t=1.65 \text{ deg kV}^{0.7}$ . From Eq. (5) it follows that the ratio of the characteristic angle is constant, i.e.,  $\psi_c/\sigma_t=1.75$ . We note that the exponent in Eq. (5) is adjustable, but with a rather narrow variance. In the previous study of the scaling laws [28,34] the exponents in Eq. (5) were slightly different, i.e., 0.65 instead of 0.7. We are convinced that the present exponent of 0.7 is more adequate, as an extended range of  $(q/E_p)^{1/2}$  values was used for the fit procedure.

Figure 6(a) shows that the universal curve reproduces all experimental results for the guiding angle within the experimental uncertainties. In fact, the guiding angle is determined with high accuracy, since the transmitted ion fraction is governed by an exponential function depending on the square of the guiding angle; see Eq. (2). A small variation in the guiding angle strongly affects the transmitted intensity. Hence, the uncertainties in  $\psi_c$  are estimated to be less than 10%.

Similarly, the transmission profile depends exponentially on the square of the width  $\sigma_t$ . The uncertainties of  $\sigma_t$  are about 15%. We note that the profile widths, presented in Fig. 6, are obtained with a nonzero tilt angle. Also, it should be realized that the observed width  $\sigma_t$  for the high projectile energies (Fig. 4) are comparable with the width of  $0.4^\circ$  measured for the incident beam (see Sec. III). Thus, the measured profile width was subtracted in quadrature by the beam width. This procedure affected primarily the profile width for the highest energy of 50 keV. After this reduction we obtained a profile width, which is in good agreement with the universal curve.

Scaling formula (5) can be deduced from Eq. (3) with the assumption of a  $(q/E_p)^{0.4}$  dependence of the potentials  $U$  and  $U_t$ . The equal  $q/E_p$  dependencies imply a constant ratio  $U_t/U=0.12$  of the effective potentials in the capillaries. Hence, the potential  $U_t$  in the exit region is nearly an order of magnitude smaller than the potential  $U$  in the entrance region. For instance, at  $(q/E_p)^{1/2}=1 \text{ kV}^{-1/2}$  the potentials were determined to be  $U=2.3 \text{ V}$  and  $U_t=0.29 \text{ V}$ . This difference in the potentials is plausible, since the main charge patch is deposited in the entrance region of the capillaries. The charge transported further inside the capillary is expected to be smaller [34].

Finally, we compare the predictions of the scaling laws with results from other laboratories. The early measurements using PET [4] yielded a relatively large guiding angle and profile width, exceeding the present scaling law by nearly a factor of 2. The guiding angles obtained by Víkor *et al.* [10] with PET and Juhász *et al.* [19] with  $\text{Al}_2\text{O}_3$  are consistent with the scaling law. The guiding angles measured with  $\text{SiO}_2$  by Sahana *et al.* [14] and with  $\text{Al}_2\text{O}_3$  by Skog *et al.* [17] are

significantly smaller (by about a factor of 2.5) than those predicted here. We recall that small changes of the guiding angle strongly affect the transmitted ion fraction.

Recently, Li *et al.* [13] using a PC polymer measured a guiding angle of  $12.6^\circ$  for 40 keV  $\text{Xe}^{7+}$  ions. This value is unexpected, since it is more than an order of magnitude higher than the results of the scaling law and the present experiment. Recall that with PC capillaries the guiding angle of  $0.78^\circ$  was obtained here for 50 keV  $\text{Ne}^{7+}$ , which has nearly the same properties as 40 keV  $\text{Xe}^{7+}$ . (Note that the scaling law is independent of the projectile mass).

For 150 nm capillaries, used in the previous experiments [13], we would expect a voltage breakthrough limit of  $\sim 15 \text{ V}$  (see Sec. III). With 40 keV  $\text{Xe}^{7+}$  ions the perpendicular energy for the incident angle of  $12.6^\circ$  is equal to  $E_\perp=1.9 \text{ keV}$ . To deflect these ions with the charge state of 7, the potential of 272 V would be needed in the entrance region. This potential appears unrealistic, as it is a factor of  $\sim 20$  higher than the estimated value for the voltage breakthrough.

## VI. DISCUSSION AND CONCLUSION

In this work we study capillary guiding of multiply charged ions, which has received a remarkable attention in the past few years. The present work is devoted to two major goals. First, the scaling laws for the characteristic angles  $\psi_c$  and  $\sigma_t$  are extended for relatively high projectile energies, for which no previous data have been available. Second, the characteristic angles were determined for capillaries in the different polymers to study the effect of the capillary material. The present work provides clear conclusions: (i) the high-energy data follow the same scaling laws as established previously and (ii) the results for the polymers PET and PC are the same within the experimental uncertainties.

Particularly, in accordance with previous studies [28,34], it was shown that the characteristic angles can be scaled by the charge-to-energy ratio of the projectile. This is plausible since  $q/E_p$  is a well-known scaling parameter for ion trajectories in an electrostatic field. We deduced the explicit  $(q/E_p)^{0.7}$  dependence for the angles  $\sigma_t$  and  $\psi_c$ , which is likely to be created by a (weak)  $(q/E_p)^{0.4}$  dependence of the potentials  $U_t$  and  $U$ . This finding may be explained by screening effects. Ions incident at higher energies penetrate more deeply the surface, resulting in a reduction in the charge available for the creation of the deflection fields  $U$  and  $U_t$  [28].

The observation of the constant ratio of the potentials  $U$  and  $U_t$  suggests that both potentials are affected by the same screening effect. This provides evidence that the potentials in the entrance and exit regions are produced by essentially the same charge near the entrance patch. Indeed, this conclusion is relevant for capillaries of higher densities  $\geq 10^8 \text{ cm}^{-2}$  [28]. For such densities the cumulated effect of the charges in adjacent capillaries is expected to play a role [26]. The charge patches in neighboring capillaries increase the field in the exit region, while they barely affect the field in the corresponding entrance region.

However, the field increase by adjacent charge patches is not likely for capillaries of low density. The present experi-

ments were performed using relatively low capillary densities of  $\approx 10^7 \text{ cm}^{-2}$  so that the entrance patches of neighboring capillaries are expected to play a minor role. In this case, the charges transported in the direction of the exit region govern the exit potential. Thus, as shown recently [34], for low capillary densities the width of the transmission profiles may not be proportional to the corresponding guiding angle. Nevertheless, it appears that for decreasing profile width the guiding angle decreases, too.

Also, the guiding angle for materials other than PET and PC may deviate from the present results. Indeed, some of the characteristic angles reported in the literature exhibit significant discrepancies. The guiding angle for a given  $q/E_p$  ratio is governed by the ability of the material to store charges in the entrance region, which, in turn, is affected by the conductivity of the material. For instance, the same PET samples used at different laboratories yielded significantly different guiding angles due to differences in the surface treatments [32]. Also, as noted in Ref. [14],  $\text{SiO}_2$  has a somewhat larger

electrical conductivity, which may limit the charge collection in the entrance patch and, hence, may be responsible for the small guiding power and exit width observed. We suggest further work to investigate the influence of the material and its surface treatment on the guiding properties. In particular, it would be favorable to find materials which meet the need for an enhanced guiding power and sharpness of the transmission profile.

#### ACKNOWLEDGMENTS

We thank Dr. D. Fink and P. Szimkowiak for preparing the PET capillaries. B.S. and Z.J. were supported by the Hungarian National Science Foundation OTKA (Grants No. K73703 and No. PD050000). This experiment was performed at the distributed LEIF-Infrastructure at ZERNIKE-LEIF. The work was financially supported by the European Network ITSLEIF Grant No. RII3-026015.

- 
- [1] Y. Yamazaki, Phys. Scr. **T73**, 293 (1997).
- [2] S. Ninomiya, Y. Yamazaki, F. Koike, H. Masuda, T. Azuma, K. Komaki, K. Kuroki, and M. Sekiguchi, Phys. Rev. Lett. **78**, 4557 (1997).
- [3] K. Tökési, L. Wirtz, C. Lemell, and J. Burgdörfer, Phys. Rev. A **61**, 020901(R) (2000).
- [4] N. Stolterfoht, J. H. Bremer, V. Hoffmann, R. Hellhammer, D. Fink, A. Petrov, and B. Sulik, Phys. Rev. Lett. **88**, 133201 (2002).
- [5] N. Stolterfoht, V. Hoffmann, R. Hellhammer, D. Fink, A. Petrov, Z. D. Pešić, and B. Sulik, Nucl. Instrum. Methods Phys. Res. B **203**, 246 (2003).
- [6] N. Stolterfoht, R. Hellhammer, Z. D. Pešić, V. Hoffmann, J. Bundesmann, A. Petrov, D. Fink, and B. Sulik, Vacuum **73**, 31 (2004).
- [7] N. Stolterfoht, R. Hellhammer, Z. D. Pešić, V. Hoffmann, J. Bundesmann, A. Petrov, D. Fink, B. Sulik, M. Shah, K. Dunn, J. Pedregosa, and R. W. McCullough, Nucl. Instrum. Methods Phys. Res. B **225**, 169 (2004).
- [8] R. Hellhammer, P. Sobocinski, Z. D. Pešić, D. Fink, J. Bundesmann, B. Sulik, and N. Stolterfoht, Nucl. Instrum. Methods Phys. Res. B **232**, 235 (2005).
- [9] R. Hellhammer, P. Sobocinski, Z. D. Pešić, D. Fink, J. Bundesmann, B. Sulik, and N. Stolterfoht, Nucl. Instrum. Methods Phys. Res. B **233**, 213 (2005).
- [10] Gy. Víkor, R. T. Rajendra Kumar, Z. Pešić, N. Stolterfoht, and R. Schuch, Nucl. Instrum. Methods Phys. Res. B **233**, 218 (2005).
- [11] Y. Kanai, M. Hoshino, T. Kambara, T. Ikeda, R. Hellhammer, N. Stolterfoht, and Y. Yamazaki, Nucl. Instrum. Methods Phys. Res. B **258**, 155 (2007).
- [12] M. Fürsatz, W. Meissl, S. Pleschko, I. C. Gebeshuber, N. Stolterfoht, H. P. Winter, and F. Aumayr, J. Phys.: Conf. Ser. **58**, 319 (2007).
- [13] D. Li, Y. Wang, Y. Zhao, G. Xiao, D. Zhao, Z. Xu, and F. Li, Nucl. Instrum. Methods Phys. Res. B **267**, 469 (2009).
- [14] M. B. Sahana, P. Skog, G. Víkor, R. T. Rajendra Kumar, and R. Schuch, Phys. Rev. A **73**, 040901(R) (2006).
- [15] S. Mátéfi-Tempfli, M. Mátéfi-Tempfli, L. Piraux, Z. Juhász, S. Biri, É. Fekete, I. Iván, F. Gáll, B. Sulik, G. Víkor, J. Pálinkás, and N. Stolterfoht, Nanotechnology **17**, 3915 (2006).
- [16] H. F. Krause, C. R. Vane, and F. W. Meyer, Phys. Rev. A **75**, 042901 (2007).
- [17] P. Skog, I. L. Soroka, A. Johansson, and R. Schuch, Nucl. Instrum. Methods Phys. Res. B **258**, 145 (2007).
- [18] X.-M. Chen, F.-Y. Xi, X.-Y. Qiu, J.-X. Shao, Y. Cui, G.-Z. Sun, J. Wang, Y.-F. Chen, H.-P. Liu, Y.-Z. Yin, F.-J. Lou, X.-A. Wang, J.-K. Xu, and C.-L. Zhou, Chin. Phys. Lett. **25**, 4348 (2008).
- [19] Z. Juhász, B. Sulik, S. Biri, I. Iván, K. Tökési, É. Fekete, S. Mátéfi-Tempfli, M. Mátéfi-Tempfli, G. Víkor, E. Takács, and J. Pálinkás, Nucl. Instrum. Methods Phys. Res. B **267**, 321 (2009).
- [20] A. R. Milosavljević, G. Víkor, Z. D. Pešić, P. Kolarž, D. Šević, B. P. Marinković, S. Mátéfi-Tempfli, M. Mátéfi-Tempfli, and L. Piraux, Phys. Rev. A **75**, 030901(R) (2007).
- [21] S. Das, B. S. Dassanayake, M. Winkworth, J. L. Baran, N. Stolterfoht, and J. A. Tanis, Phys. Rev. A **76**, 042716 (2007).
- [22] T. Ikeda, T. M. Kojima, Y. Iwai, Y. Kanai, T. Kambara, T. Nebiki, T. Narusawa, and Y. Yamazaki, J. Phys.: Conf. Ser. **58**, 68 (2007).
- [23] A. Cassimi, T. Muranaka, L. Maunoury, H. Lebius, B. Manil, B. A. Huber, T. Ikeda, Y. Kanai, T. M. Kojima, Y. Iwai, T. Kambara, Y. Yamazaki, T. Nebiki, and T. Narusawa, Int. J. Nanotechnol. **5**, 809 (2008).
- [24] R. Bereczky, G. Kowarik, F. Aumayr, and K. Tökési, Nucl. Instrum. Methods Phys. Res. B **267**, 317 (2009).
- [25] K. Schiessl, W. Palfinger, C. Lemell, and J. Burgdörfer, Nucl. Instrum. Methods Phys. Res. B **232**, 228 (2005).
- [26] K. Schiessl, W. Palfinger, K. Tökési, H. Nowotny, C. Lemell, and J. Burgdörfer, Phys. Rev. A **72**, 062902 (2005).
- [27] N. Stolterfoht, R. Hellhammer, J. Bundesmann, D. Fink, Y.

- Kanai, M. Hoshino, T. Kambara, T. Ikeda, and Y. Yamazaki, *Phys. Rev. A* **76**, 022712 (2007).
- [28] N. Stolterfoht, R. Hellhammer, J. Bundesmann, and D. Fink, *Phys. Rev. A* **77**, 032905 (2008).
- [29] P. Skog, HQ. Zhang, and R. Schuch, *Phys. Rev. Lett.* **101**, 223202 (2008).
- [30] Y. Kanai, M. Hoshino, T. Kambara, T. Ikeda, R. Hellhammer, N. Stolterfoht, and Y. Yamazaki, *Phys. Rev. A* **79**, 012711 (2009).
- [31] N. Stolterfoht, R. Hellhammer, D. Fink, B. Sulik, Z. Juhász, E. Bodewits, H. M. Dang, and R. Hoekstra, *Phys. Rev. A* **79**, 022901 (2009).
- [32] N. Stolterfoht, R. Hellhammer, J. Bundesmann, and D. Fink, *Radiat. Eff. Defects Solids* **162**, 515 (2007).
- [33] R. Hellhammer, J. Bundesmann, D. Fink, and N. Stolterfoht, *Nucl. Instrum. Methods Phys. Res. B* **258**, 159 (2007).
- [34] N. Stolterfoht, R. Hellhammer, J. Bundesmann, and D. Fink, *Nucl. Instrum. Methods Phys. Res. B* **267**, 226 (2009).
- [35] M. Unipan, A. Robin, D. F. A. Winters, R. Morgenstern, and R. Hoekstra, *Phys. Rev. A* **74**, 062901 (2006).
- [36] G. Pépy, P. Boeseck, A. Kuklin, E. Manceau, B. Schiedt, Z. Siwy, M. Toulemonde, and C. Trautmann, *J. Appl. Crystallogr.* **40**, s388 (2007).